

In the format provided by the authors and unedited.

Ultra-low-threshold continuous-wave and pulsed lasing in tensile-strained GeSn alloys

Anas Elbaz^{1,2}, Dan Buca³✉, Nils von den Driesch^{3,4}, Konstantinos Pantzas¹, Gilles Patriarche¹, Nicolas Zerounian¹, Etienne Herth¹, Xavier Checoury¹, Sébastien Sauvage¹, Isabelle Sagnes¹, Antonino Foti⁵, Razvigor Ossikovski⁵, Jean-Michel Hartmann⁶, Frédéric Boeuf², Zoran Ikonik⁷, Philippe Boucaud⁸, Detlev Grützmacher^{3,4} and Moustafa El Kurdi¹✉

¹Center for Nanoscience and Nanotechnology, C2N UMR 9001, CNRS, Université Paris Sud, Université Paris Saclay, Palaiseau, France. ²STMicroelectronics, Crolles, France. ³Peter Grünberg Institute (PGI 9) and JARA-Fundamentals of Future Information Technologies, Forschungszentrum Juelich, Juelich, Germany. ⁴JARA-Institute Green IT, RWTH Aachen, Aachen, Germany. ⁵LPICM, CNRS, Ecole Polytechnique, Université Paris-Saclay, Palaiseau, France. ⁶CEA, LETI and Univ. Grenoble Alpes, Grenoble, France. ⁷Pollard Institute, School of Electronic and Electrical Engineering, University of Leeds, Leeds, UK. ⁸Université Côte d'Azur, CNRS, CRHEA, Valbonne, France. ✉e-mail: d.m.buca@fz-juelich.de; moustafa.el-kurdi@u-psud.fr

Supplementary information

Ultra-low threshold continuous-wave and pulsed lasing in tensile strained GeSn alloys

Anas Elbaz^{1,2}, Dan Buca^{3,*}, Nils von den Driesch^{3,4}, Konstantinos Pantzas¹, Gilles Patriarche¹, Nicolas Zerounian¹, Etienne Herth¹, Xavier Checoury¹, Sébastien Sauvage¹, Isabelle Sagnes¹, Antonino Foti⁵, Razvigor Ossikovski⁵, Jean-Michel Hartmann⁶, Frédéric Boeuf², Zoran Ikonc⁷, Philippe Boucaud⁸, Detlev Grützmacher^{3,4}, and Moustafa El Kurdi^{1,*}

¹ Center for Nanoscience and Nanotechnology, C2N UMR 9001, CNRS, Université Paris Sud, Université Paris Saclay, 91120 Palaiseau, France

² STMicroelectronics, Rue Jean Monnet 38054 Crolles, France

³ Peter Grünberg Institute (PGI 9) and JARA-Fundamentals of Future Information Technologies, Forschungszentrum Juelich, 52428 Juelich, Germany

⁴ JARA-Institute Green IT, RWTH Aachen, 52062 Aachen, Germany

⁵ LPICM, CNRS, Ecole Polytechnique, Université Paris-Saclay, 91128 Palaiseau, France

⁶ CEA, LETI and Univ. Grenoble Alpes, 38054 Grenoble, France

⁷ Pollard Institute, School of Electronic and Electrical Engineering, University of Leeds, Leeds LS2 9JT, UK

⁸ Université Côte d'Azur, CNRS, CRHEA 06560 Valbonne, France

*corresponding author: moustafa.el-kurdi@u-psud.fr, d.m.buca@fz-juelich.de

Table of contents:

- 1. Material characterization**
- 2. Processing and strain engineering**
- 3. Microdisk emission for different strain / technology steps**
- 4. Photoluminescence comparison and optical transitions assignment**
- 5. Thermal heating modelling**
- 6. Lasing spectra and threshold analysis**
- 7. Modal gain assuming SRH model**
- 8. Steady-state electron distribution in conduction band versus temperature**

1. Material characterization

Transmission electron microscopy (TEM) was used to investigate the crystalline and structural quality of the GeSn layer. A lamella was prepared using focused ion beam (FIB) and observed in a FEI Titan TEM microscope operating at 200 keV. Figure SI-1a shows a high-angle annular dark field (HAADF) Scanning TEM (STEM) micrograph of the GeSn layer. The 260 nm thick GeSn layer is partially relaxed through the formation of dislocations at the Ge/GeSn interface. These dislocations are localized within the first 20 nm of the GeSn layer as shown in the dark-field TEM micrograph in Figure SI-1b. No threading dislocations (TDs) were observed in TEM micrograph, so the lower limit for the TDs density is taken equal to the TDs density in the Ge-VS, $1 \times 10^7 \text{ cm}^{-2}$. A detailed analysis of TD density in Ge-VS was performed in Ref. [1].

The composition of the layer was measured by Rutherford Backscattering Spectrometry (RBS) and energy dispersive X-ray (EDX) spectroscopy. The plot in Figure SI-1c shows the results of these measurements along the growth direction. The average composition of the layer is 5.4 at.% of Sn, in agreement with Rutherford Backscattering Spectrometry (not shown here). A small gradient of Sn content of 0.7 % seems to be present along the growth direction, attributed to the strain relaxation of the layer. The GeSn layer is, therefore, slightly richer in Sn close to the surface contributing to carrier diffusion from the defective Ge/GeSn interface region towards the layer interior.

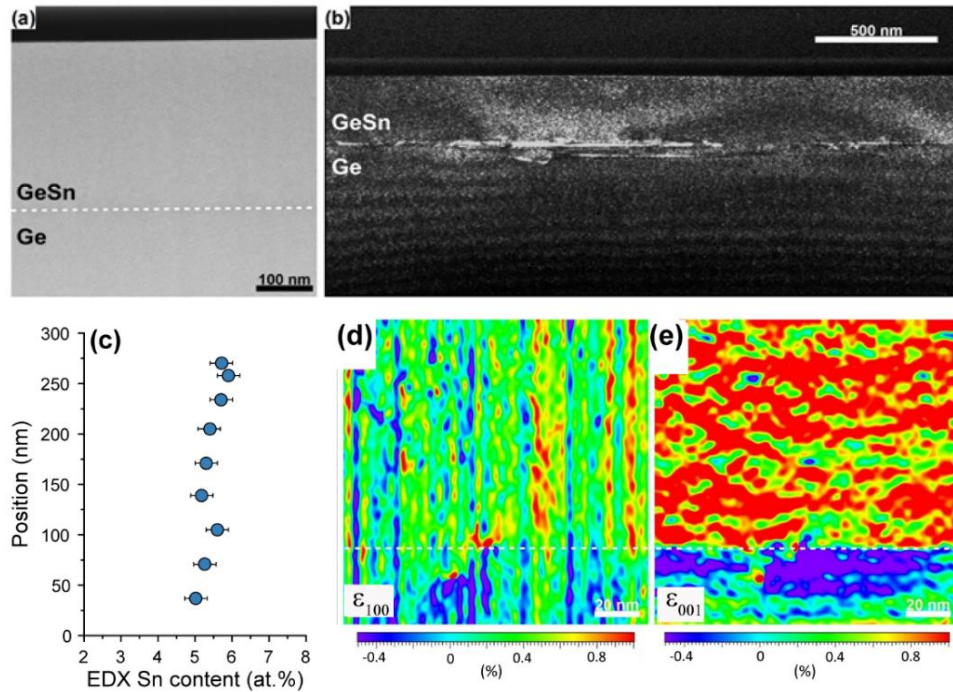


Figure SI-1. (a) High-angle annular dark field STEM micrograph of the as-grown 260 nm GeSn layer. (b) Dark-field TEM micrograph showing the presence of dislocations at the interface. (c) EDX line-scan along the growth direction, indicating an average Sn content of 5.4 at.%. A slight gradient of -0.7 at.% over 260 nm of the GeSn layer depth is observed. (d), (e) Strain mapping in the in-plane and out-of-plane directions, as obtained from Geometric Phase Analysis using bright field-STEM. The average in-plane and out-of-plane deformation with respect to Ge are $0.3\% \pm 0.3\%$ and $0.9\% \pm 0.5\%$, respectively. The (in-

plane) material strain calculated from these data is $-0.5\% \pm 0.3\%$.

Geometric Phase Analysis (GPA) was used to evaluate the strain distribution in the GeSn layer, delivering information on local strain with respect to the Ge-VS template. The findings are summarized in Figure SI-1d,e. The average in-plane deformation with respect to Ge is $0.3\% \pm 0.3\%$ while the out-of-plane one is $0.9\% \pm 0.5\%$, showing that GeSn has a tetragonal structure, being partially strain relaxed. The strain calculated from the lattice deformation (w.r.t. cubic GeSn crystal) for Sn content of 5.4 at.% is $-0.5\% \pm 0.3\%$, in reasonable agreement with XRD measurements (Figure 1 in the manuscript). The Z contrast of the GeSn layer is highly homogeneous, indicating that Sn atoms are evenly distributed.

2. Processing and strain engineering

The GeSn layers were processed into microdisks, embedded in a silicon nitride (SiN_x) stressor. The process, somewhat similar to that used for the fabrication of SOI substrates, was adapted to take three aspects into account: i) a stressor layer is included; ii) a heat sink layer is added; and iii) the materials/processes are chosen such that their deposition/processing temperature is below the growth temperature of the GeSn layer. The technological flow is schematically illustrated in Figure SI-2. On the as-grown GeSn on Ge-VS, a 350 nm thick SiN_x layer is deposited by plasma-enhanced chemical vapor deposition (PECVD), followed by 1 μm of aluminum (Al), deposited by e-beam evaporation (Fig. SI-2a). While multiple choices, such as SiO_2 - SiO_2 or Al-Al, are available for bonding, Au-Au bonding process was used in this proof-of-concept work. In order to avoid Au diffusion into Al during bonding at 320°C , a 100 nm SiN_x diffusion barrier was deposited by PECVD. The layers stack prior bonding is shown in Fig SI-2b. The total thermal budget for bonding and subsequent annealing, to increase the bonding strength, was maintained low enough to ensure the integrity of the GeSn layer by avoiding Sn segregation. Additionally, further relaxation of the GeSn layer is avoided.

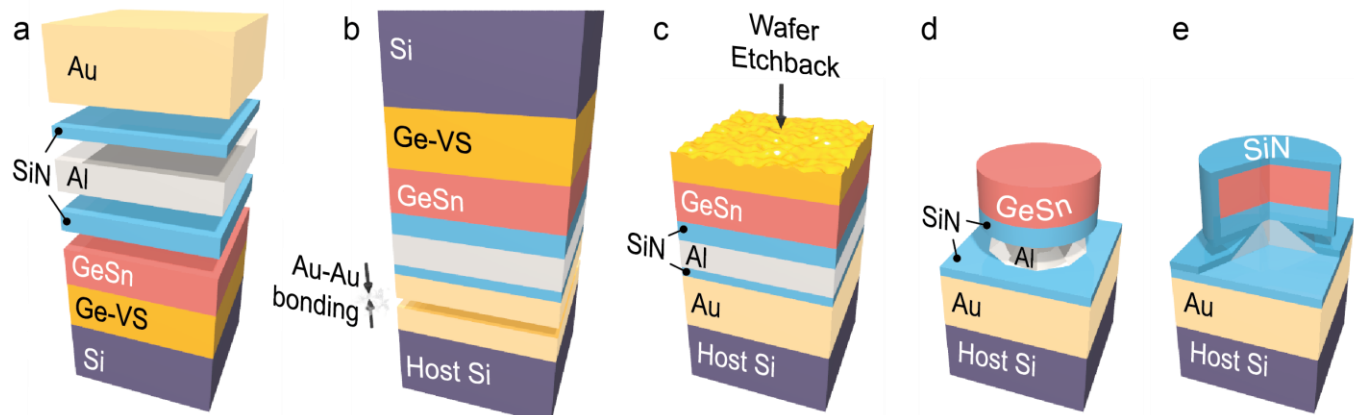


Figure SI-2: (a)-(d) Schematic view of the process flow, illustrating different fabrication steps of the strained GeSn disk. (a) Layer stack prior to bonding. (b) Bonding process. (c) Back-etching of the donor wafer. (d) Formation of the suspended disk by under-etching of the Al layer. At this step the strain from the bottom SiN stressor is transferred into the GeSn. (e) Final device structure: GeSn embedded in SiN .

Most of the Si substrate is removed by chemical mechanical polishing (CMP) down to 50 μm thickness followed by a selective wet etching of the remaining Si substrate. The Ge-VS layer acts as etch-

stop, having a very large etch selectivity versus Si in KOH wet chemical solution. A sulfur hexafluoride (SF_6) plasma is then used to remove the 2.5 μm thick Ge-VS (Figure SI-2c). At this step, about 40 nm of the GeSn layer, including the defective interface with Ge-VS, is also etched away. The GeSn layer thickness is reduced from 300 nm down to 260 nm. This transferred layer is then processed by standard lithography to define microdisk mesas with diameters in the range 4-9 μm . The mesas were etched into the GeSn/ SiN_x stack down to Al layer by Cl_2 plasma in a reactive ion etching system. The choice of Al for the metal was dictated by the high selectivity of KOH in etching Al versus GeSn and SiN_x , allowing for a precise under-etch control and, thus, tuning of the strain transferred into the GeSn layer. At the same time, large Al pillars are targeted to allow for an efficient heat sink. The suspended microdisk structure is shown in Fig. SI-2d. Once the metallic post was defined, a second SiN_x stressor layer (intrinsic stress of -1.9 GPa) is conformally deposited by PECVD, resulting in a GeSn microdisk embedded in SiN_x (Figure SI-2e). The top SiN_x is 400 nm and the bottom layer 350 nm thick.

3. Microdisk emission for different strain / technology steps

From the as-grown layer to the all-around disk different strain condition can be obtained. We can indeed fabricate the disk directly from the as-grown layer, then one should get a strain-free suspended GeSn layer cavity. A detailed analysis of strain in such a structure was performed in Ref. [2]. As shown in figure SI-3, with the material being an indirect band gap semiconductor the lasing cannot be reached, even under high pulsed pump power.

The next device is obtained following the steps shown in Fig SI-2, ending with the structure in FigSI2-d. The result is GeSn layer bonded on a SiN_x layer. The PL of the microdisk shows a red shift and a strong enhancement of the emission as compared to the as-grown layer disk. The red shift is a signature of tensile strain induced by the underlying SiN_x after patterning. In this case no laser effect can be obtained, either. The tensile strain is expected to be highly inhomogeneously distributed both along the disk diameter and across the layer depth. A detailed analysis of single side stressor layer on the disk is performed in Ref. [3]. FEM analysis shows that the average biaxial tensile strain in the layer is 0.5%, with the maximal strain of 0.8% close the GeSn/ SiN interface. In this strain configuration we were not able to get lasing, although the defects removal has been performed. Finally after the formation of an all-around SiN structure, by additional deposition of a second 400 nm SiN_x stressor layer on top of the previous structure, the lasing is achieved. The tensile strain reaches 1.4%, and has a highly homogenous volume distribution. This is the case discussed in the manuscript.

The results presented above referred to a $\text{Ge}_{0.946}\text{Sn}_{0.054}$ layer that is an indirect gap semiconductor for as-grown bulk conditions. The processing performed here can, however, offer laser emission for other (Sn composition - strain value) combinations, if it turns into a direct bandgap semiconductor and close to it.

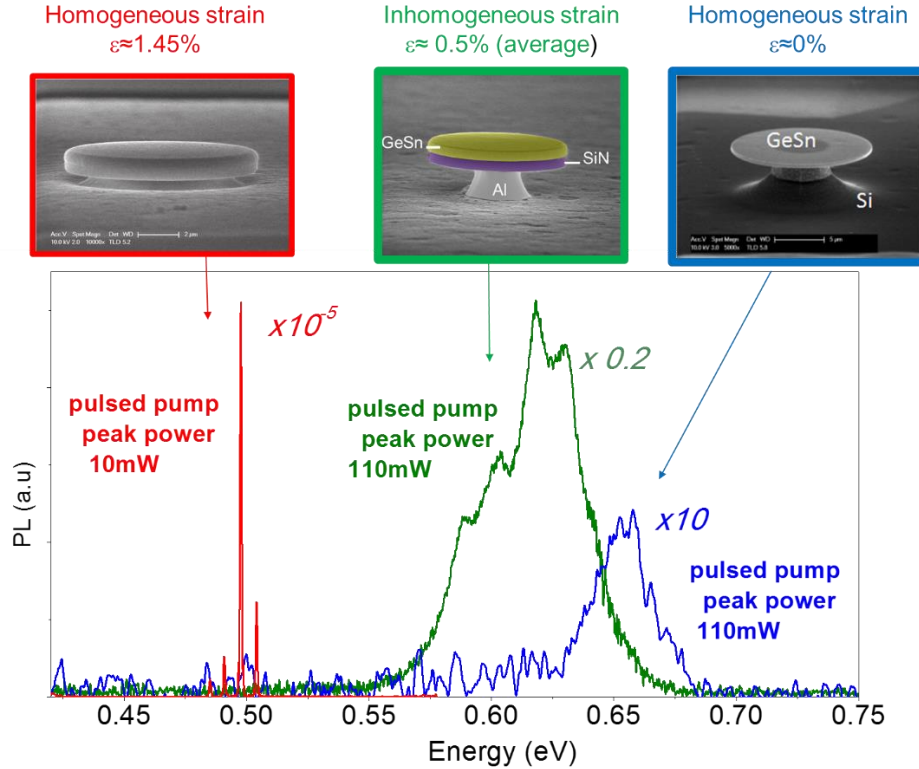


Figure SI-3: Photoluminescence analysis under pulsed pumping for different strain conditions in the GeSn layer used in this work i) suspended relaxed disk, ii) transferred layer with a single-bottom side SiN_x layer, iii) GeSn encapsulated in the all-around SiN_x stressor.

4. Photoluminescence comparison and optical transitions assignment

Figure 1 in the manuscript shows PL emission of the layer in the as-grown and bonded (but still unpatterned) form, measured by a highly sensitive InGaAs detector. For measurements of the final, tensile-strained device, a liquid nitrogen cooled InSb detector with a longer cut-off wavelength was used. Here we show the PL emission of the bonded layer and the final structure, GeSn disk embedded in SiN layers, using the InSb detector (Figure SI-4). This detector's sensitivity is, however, lower than that of InGaAs, making it less suitable for detection of emission from the as-grown layer. A large red-shift and a strong PL emission enhancement (about two orders of magnitude) are observed. These changes are attributed to a tensile strain induced band-gap narrowing and to the change from an indirect to direct character of the fundamental band-gap.

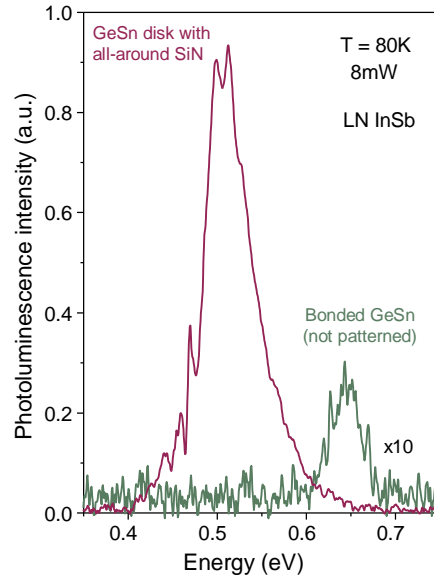


Figure SI-4: The PL emission at 80K of the GeSn layer: (green) after bonding (no strain transfer) and GeSn/Ge-VS interface etch, the direct transition Γ -HH dominates the spectrum; (pink) final structure: tensile strained GeSn embedded in SiN.

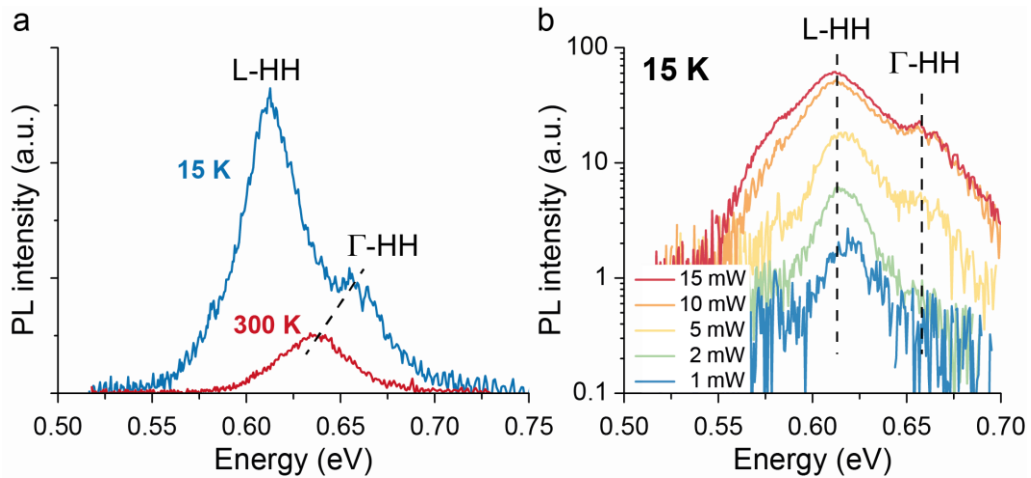


Figure SI-5: (a). Temperature dependence of the PL spectra of the bonded layer. The indirect transition L-HH dominates at 20K and the direct transition Γ -HH at 300K. (b) PL power dependence of the layer at low temperature, 15K.

In thin layers the PL at room temperature is dominated by the direct transitions for both indirect and direct bandgap semiconductors. In our case, with the compressive $\text{Ge}_{0.946}\text{Sn}_{0.054}$ layer, this is the Γ -HH optical transition. The major difference in PL between indirect and direct semiconductors is seen at low T and through the temperature behaviour. At cryogenic temperatures, the electrons occupy the lowest energy band, which is the L -valley for an indirect semiconductor and Γ -valley for a direct one. For our indirect GeSn compressively strained layer at 15K the main PL emission comes from the fundamental L-HH optical transition. The Γ -HH optical transition can be observed when the Γ -valley starts to be populated. This can be obtained:

- 1- Under high pumping conditions. This is shown in Fig. SI-5b. For our $\text{Ge}_{0.946}\text{Sn}_{0.054}$ layer this happens above 5mW.
- 2- Increasing the temperature. The electrons will be thermally activated to populate the Γ -conduction band. This thermal activation to direct conduction band occurs already at 80K due to the small energy difference between the L- and the Γ -valley, as extracted from the k.p modeling. Also very important is that the oscillator strength for direct transition is orders of magnitude larger than for the indirect transition. This makes the direct transition dominate over the indirect one at 80K and above.

Based on the above PL temperature behaviour we can conclude that the $\text{Ge}_{0.946}\text{Sn}_{0.054}$ layer under -0.32% compressive strain is an indirect semiconductor and assign the peak at 0.61 eV to the indirect L-HH fundamental optical transition and the higher energy peak at 0.66 eV to the Γ -HH direct optical transition. This energy difference of 50 meV is comparable to the Γ -L energy difference of 60 meV predicted by modeling.

5. Thermal heating modeling

Modelling of the thermal heat distribution inside the GeSn disk under optical pumping was performed using the same procedure, based on Finite Element Modeling (FEM), as in Ref. [4]. The pump power absorbed by the active layer is set as a homogeneous heat source distributed on the disk surface. A factor of 0.65 applied to the incident power takes into account the GeSn surface reflectivity at the pump wavelength of 1550 nm. Under 8 mW of incident power focused into a 12 μm spot diameter the intensity is 7.1 kW/cm^2 . The all-integrated absorbed power by the 9 μm diameter is thus 2.9 mW within the active GeSn layer, out of the total cw incident power of 8 mW. We assume that all the absorbed power is converted into heat in the disk. The FEM modeling results are shown in figure SI-6a. The data for GeSn thermal conductivity are scarce in the literature, but Sn alloying generally induces a significant drop in thermal conductivity due to mass disorder induced phonon scattering. In Fig SI-6b the modelling was performed for GeSn thermal conductivities of $1 \text{ Wm}^{-1}\text{K}^{-1}$, $2 \text{ Wm}^{-1}\text{K}^{-1}$ and $10 \text{ Wm}^{-1}\text{K}^{-1}$. The thermal conductivity of elemental Ge is $58 \text{ Wm}^{-1}\text{K}^{-1}$.

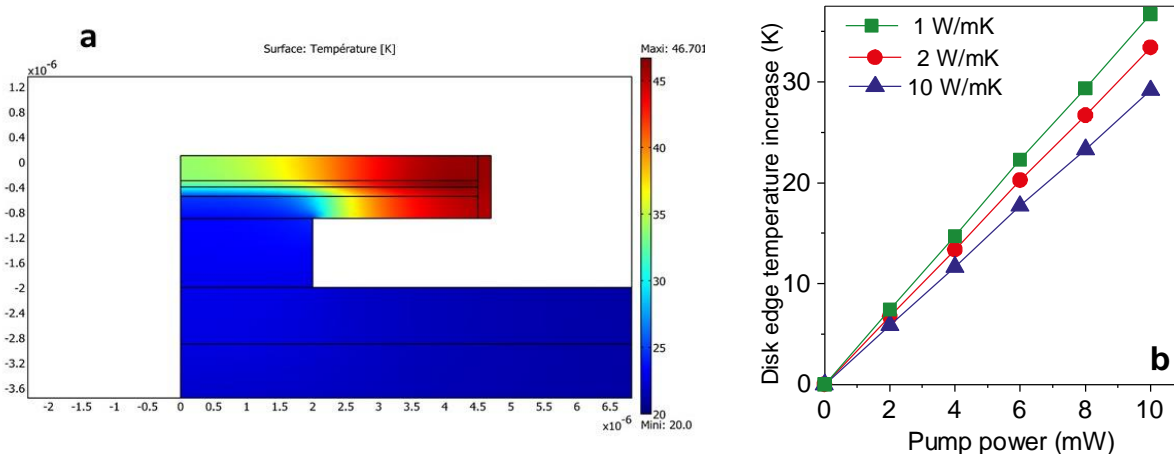


Figure SI-6: (a) Finite element modeling of temperature in the microdisk under incident pump power

of 8 mW. (b) Maximum temperature, at the disk edge, as a function of incident pump power for different GeSn thermal conductivities.

In Fig SI-6b the maximum temperature at the disk edge, where the whispering gallery modes form, is shown for different thermal conductivities. For our case of 9 μm diameter disks, a temperature increase of about 30 K under 8 mW pump power, i.e. 7.1 kW/cm^2 intensity, is found. The modeling is performed assuming a continuous heat source, and the results represent the steady-state temperature. Under pulsed pumping, the pulse duration is only 3.5 ns, very short compared to heat transfer rates out of the disk, which are in the μs range. One can thus take that the temperature reached in pulsed regime scales with the duty cycle, i.e. for a given pulsed peak power the heating is much lower than in cw. Therefore, the temperature increase under pulsed excitation, as used in this work, is estimated to be below 10 K, for pulsed peak power range of 0-100 mW. Note that due to unknown thermal transport parameters in GeSn alloy, this value should be taken as a rough estimate.

6. Lasing spectra and threshold analysis

The threshold extraction for the 9 μm disk at 20K under cw excitation and for the 12 μm diameter disk under both cw and pulsed excitations is shown in Fig SI-7 a-c. The same fabrication method was used, and also the same etching time as for the 9 μm diameter disk, to allow identical under-etch of the GeSn disk. The main difference is then only in the size of the Al pillar, directly related to the disk heat dissipation. The result is an increase of the cw lasing temperature from 45K for the 9 μm disk to 72K for the 12 μm disk. This is an increase by almost 30K for cw pumping and only 15K for pulse pumping. This indicates that cw lasing is more temperature sensitive than the pulsed lasing. In our case, the cw lasing thresholds for the 9 μm and 12 μm disk are almost identical at 20-30K. The cw and pulsed thresholds, similar at 20K, have however different temperature behaviour, and the lasing quenches faster for the cw laser. Note that the energy deposited in the disk by cw optical pumping is 11 times higher than in the pulsed pumping mode.

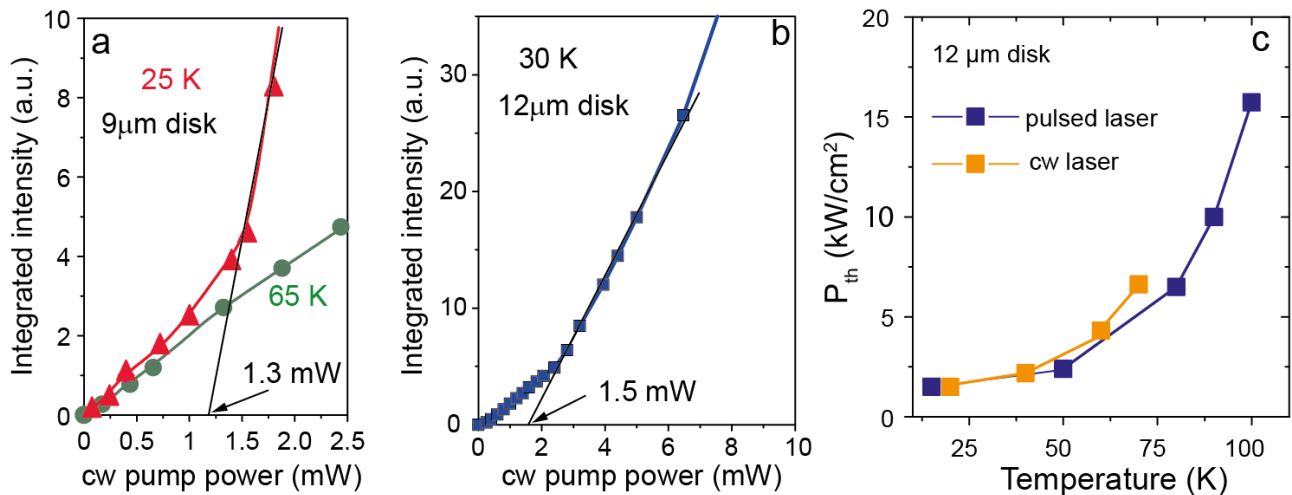


Figure SI-7: Threshold analysis for: (a) the 9 μm diameter disk under cw pumping, and (b) for the 12 μm diameter disk, showing equivalent lasing thresholds, and (c) Lasing threshold obtained for the 12 μm disk as a function of temperature and under cw and pulsed pumping. The maximum lasing operation temperature is 72 K under cw, and 100K under pulsed excitation.

The power dependence of PL emission spectra from a 12 μm disk, at the temperature of 72K are presented in Fig SI-8a. The light-in-light-out characteristics at 72K is plotted in Fig. SI-8b.

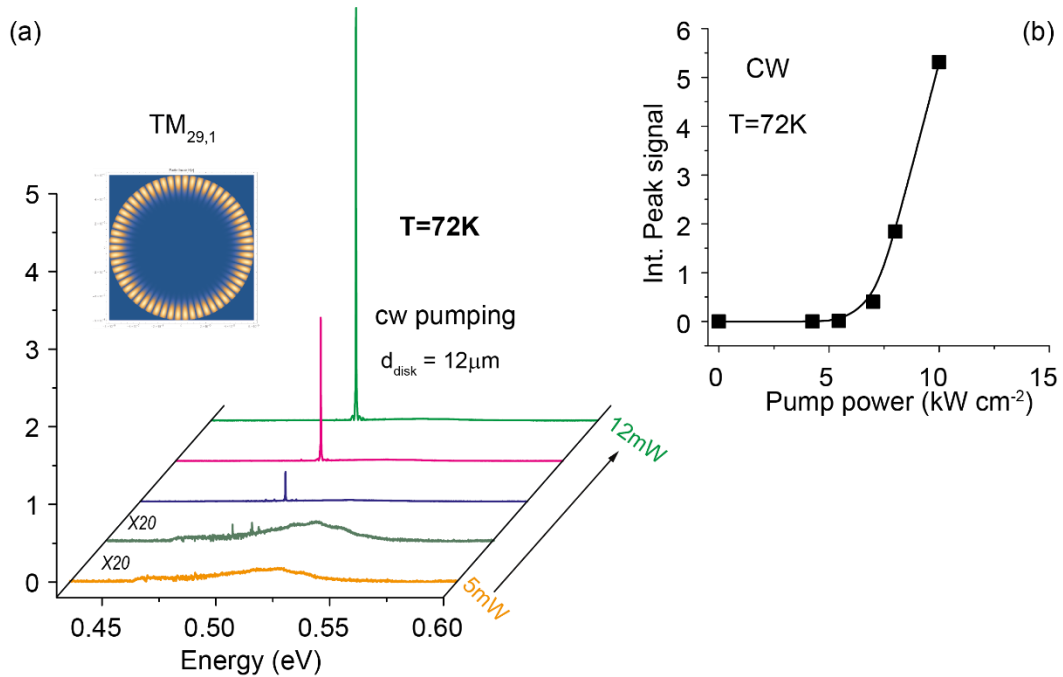


Figure SI-8: (a) The spectra and the (b) L-L curve at 72K for a 12 μm GeSn disk.

7. Modal gain assuming SRH model

To investigate the effect of thermal activation of defects on the modal gain, we perform comparative modeling of gain in two cases, shown in Figure SI-9. The energy difference $\Delta E_{L-\Gamma}$, also called directness, corresponds to the one deduced from the **k.p** modeling of the photoluminescence (70 meV). The valence band splitting ΔE_{LH-HH} amounts to 172 meV. Two cases have been considered: one, where the carrier density is kept constant at 10^{18} cm^{-3} when increasing the temperature, and the second scenario, in which the non-radiative lifetime follows the temperature dependence as given in Ref. [5]. In the first case, the gain decreases with temperature because carriers thermally transfer from Γ to the L valley. In the second case, the injected carrier density decreases with temperature also due to activation of trap levels, following the SRH model of the lifetime, and an activation energy of 19 meV was used, as in Ref. [5]. This results in the modal gain sharply decreasing above 50 K.

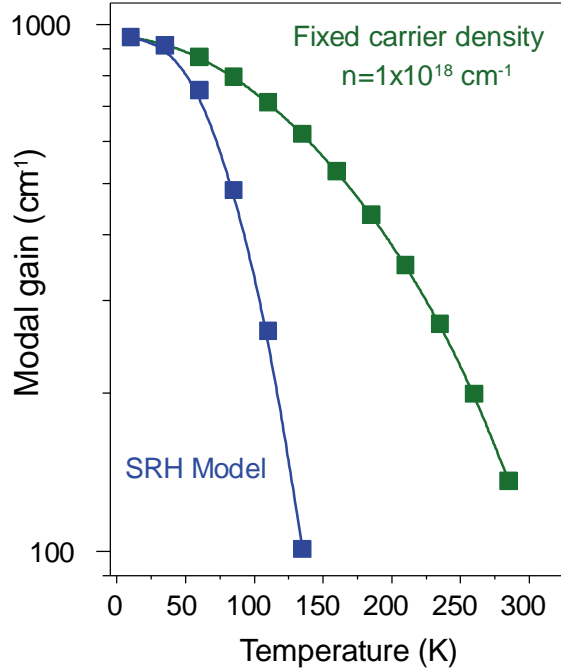


Figure SI-9: Modal gain versus temperature for two scenarios: i) the carrier density is kept constant as temperature varies, and ii) the carrier density decreases due to the SRH-like decrease of the non-radiative recombination time.

8. Steady-state electron distribution in conduction band versus temperature

The steady-state electron distribution was calculated using the band dispersion from the **k.p** model for Γ , and the effective mass based dispersion for L-valley. Figure SI-10a shows the temperature dependence of the equilibrium fraction of electron population in the Γ -valley (the remaining part being in L-valley) for an electron density in the active layer of 10^{18} cm^{-3} (as in Fig. SI-9) for two different biaxial strain values. Larger tensile strain, which increases the $\Delta E_{L-\Gamma}$ difference, is highly beneficial for Γ population, being able to compensate for the larger DOS of the L-valley. This is particularly useful at higher temperatures, where electrons can access higher DOS regions well inside the conduction band. Since only Γ electrons contribute to gain and L-electrons only bring in the free-carrier absorption, the fraction of electrons in Γ should be reasonably large. Clearly, the 1.5% tensile strain in a $\text{Ge}_{0.94}\text{Sn}_{0.06}$ alloy enables larger Γ population, as large as is achievable in relaxed or compressively strained GeSn with much larger Sn content. Increasing biaxial tensile strain to 2%, more challenging technologically, will also enable a $N_{\Gamma}/N_{\text{total}}$ population ratio over 50%, offering higher operation temperature.

While the large Sn content alloys suffer from a large density of defects/non-radiative recombination centers, too large strain may also bring in material quality issues (bulk defects, device operating lifetime). A trade-off between these two approaches needs to be found to enable room temperature lasing. Figure SI-10b shows the temperature dependent electron population fraction in Γ for different Sn contents in 1.5% tensile strained GeSn alloys, which highlights the influence of this parameter on the electron distribution in the Γ -valley. As can be seen for the case of 6 at.% Sn content, with lower $\Delta E_{L-\Gamma}$ splitting, electron population decreases rapidly with increasing temperature, as seen experimentally in the manuscript.

However medium Sn contents of 10 at.% give a larger directness, which allows larger Γ -valley population. This will increase the gain and result in higher operation temperature.

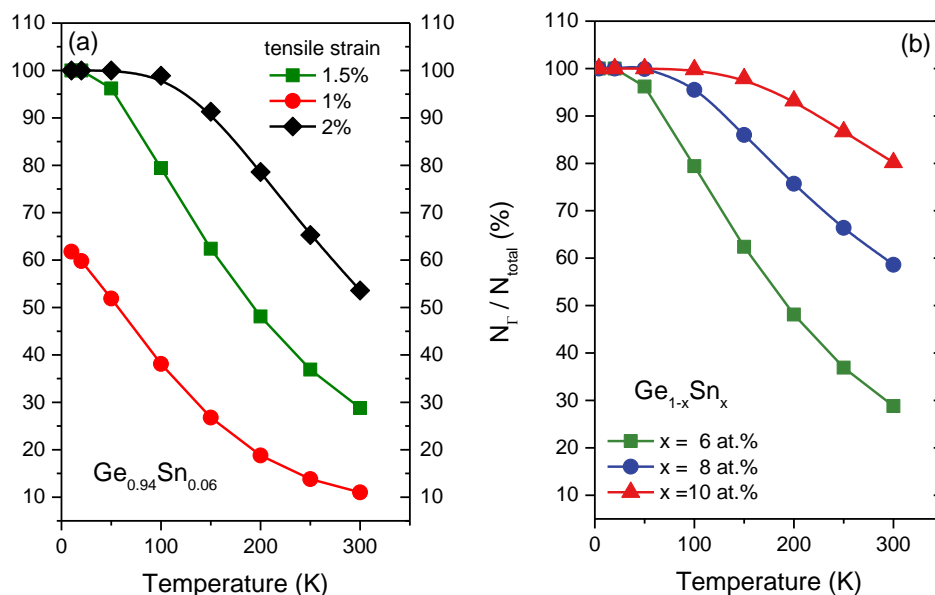


Figure SI-10: (a) Electron fraction in Γ -valley in GeSn alloy with Sn content of 6 at.% under tensile strain of 1%, 1.5% and 2%. (b) Electron fraction in Γ -valley for a tensile strain of 1.5% in GeSn alloys with Sn content of 6 at.%, 8 at.% and 10 at.%.

References

- Hartmann, J.-M., Abbadie, A., Cherkashin, N., Grampeix, H. & Clavelier, L. Epitaxial growth of Ge thick layers on nominal and 6° off Si(001); Ge surface passivation by Si. *Semicond. Sci. Technol.* **24**, 055002, DOI: [10.1088/0268-1242/24/5/055002](https://doi.org/10.1088/0268-1242/24/5/055002) (2009).
- Stange, D. et al. Optically Pumped GeSn Microdisk Lasers on Si. *ACS Photonics* **3**, 1279–1285, DOI: [10.1021/acsphotonics.6b00258](https://doi.org/10.1021/acsphotonics.6b00258) (2016)
- Ghrib, A. et al. Tensile-strained germanium microdisks. *Appl. Phys. Lett.* **102**, 221112, DOI: [0.1063/1.4809832](https://doi.org/10.1063/1.4809832) (2013).
- Elbaz, A. et al. Solving thermal issues in tensile-strained Ge microdisks. *Opt. Express* **26**, 28376–28384, DOI: [10.1364/OE.26.028376](https://doi.org/10.1364/OE.26.028376) (2018).
- Wirths, S. et al. Lasing in direct-bandgap GeSn alloy grown on Si. *Nat. Photonics* **9**, 88–92, DOI: [10.1038/nphoton.2014.321](https://doi.org/10.1038/nphoton.2014.321) (2015)